American Mineralogist, Volume 79, pages 91–106, 1994

Structure and polytypism of bementite, a modulated layer silicate

Angela R. Heinrich, Richard A. Eggleton
Australian National University, Department of Geology, Canberra, A.C.T. 0200, Australia
Stephen Guggenheim
University of Illinois at Chicago, Department of Geological Sciences, Chicago, Illinois 60680, U.S.A.

Abstract

High-resolution transmission electron microscope (HRTEM) imaging and electron diffraction, combined with powder X-ray diffraction (XRD) data and a partial powder profile analysis by the Rietveld method, have been used to determine the parent structure and the polytypism of bementite, $Mn_7Si_6O_{15}(OH)_8$, a modulated 1:1 layer silicate from Franklin, New Jersey.

The parent structure is monoclinic $P2_1/c$ with $a = 14.838(2)$, $b = 17.584(2)$, $c = 14.700(2)$ Å, and $\beta = 95.54(2)°$, $Z = 4$, $V = 3814.8$ Å^3, and $M = 929$ g/mol. It consists of two hexagonal sheets of octahedra, accommodating the Mn, which are alternately rotated by 22° in the **ab** plane. These are interlayered by a continuous tetrahedral sheet containing pairs of six-membered rings interconnected with five- and seven-membered rings. Inverted tetrahedra form strips with like orientation (up or down) parallel to **a**. Linked pairs of six-membered rings are rotated relative to pairs across strip boundaries by 22° to allow coordination with adjacent octahedral sheets.

The polytypism, which can be ascribed to an interface modulation caused by stacking faults, is best visible in HRTEM images and diffraction patterns of the [010] projection. The displacement and frequency of the faults were determined from the distribution of satellite reflections and their displacement relative to the parent reflections. Bementite can be interpreted as a combination of two basic stacking varieties of topologically identical octahedral and tetrahedral sheets. Variety I is considered the parent structure, with $\beta = 95.5°$. Variety II has a stacking error after every Mn layer, which results in $\beta = 71.3°$.

Introduction

Bementite is a modulated layer silicate, a group of minerals in which continuous trioctahedral sheets coordinate with tetrahedral sheets that have periodic inversions in the orientation of their tetrahedral apices (Guggenheim and Eggleton, 1988). The term "modulated" in the context of sheet silicates should not be confused with the more general term "modulated structure" as defined, for instance, by Cowley (1979). A modulated structure consists of two elements: the basic structure on the one hand, and the periodic perturbation of this basic structure resulting in the modulated structure, on the other hand. Modulated layer silicates may be described by a subcell, defined by the octahedral sheets only, and a supercell, defined by octahedral and tetrahedral sheets. The subcell, in general smaller and of higher symmetry than the supercell, is modulated by the apical inversions of the coordinating tetrahedral sheets. The resulting supercell represents the periodicity and symmetry of the whole structure.

The tetrahedral connections of modulated layer silicates are typically more complex than the linked hexagonal rings of normal layer silicates. Besides normal six-membered rings, they may contain three-membered rings (e.g., zussmanite: Lopes-Vieira and Zussman, 1969), four-membered rings (e.g., pyrosmalite: Kato and Takéuchi, 1983), five-membered rings (e.g., stilpnomelane: Eggleton, 1972), seven-membered rings (e.g., bannisterite: Threadgold, 1979), eight-membered rings (e.g., antigorite: Kunze, 1961), and 12-membered rings (e.g., pyrosmalite: Kato and Takéuchi, 1983). As a simple example, a sketch of the pyrosmalite structure (after Kato and Takéuchi, 1983) is shown in Figure 1.

The structural complexity of modulated layer silicates and the perturbation of their tetrahedral sheets can, as a first approximation, be related to a misfit between the lateral dimensions of the tetrahedral and the octahedral sheets. Some silicates accommodate tetrahedral-octahedral misfit by enlarging the tetrahedra through Al-Si substitution (e.g., annite). Modulated layer silicates characteristically have low ratios of $^{[4]}$Al to $^{[4]}$Si, in general combined with a high content of relatively large octahedral cations such as Fe^{2+} or Mn^{2+} (Guggenheim and Eggleton, 1987) and yet are essentially planar sheet structures. In high Fe + Mn but low Al/Si layer-silicate systems, the tetrahedral apices spread apart to compensate for the misfit. In some silicates this apical spread may result in a curling of the tetrahedral sheet (e.g., chrysotile) or in the formation of tetrahedral tubes, as in some

0003–004X/94/0102–0091$02.00

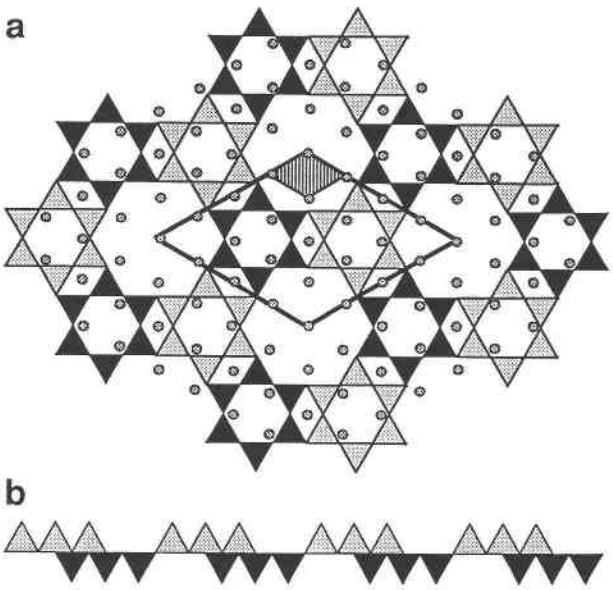

Fig. 1. Schematic drawing of the tetrahedral sheet of pyrosmalite, with tetrahedra in black pointing down and tetrahedra in gray pointing up (based on Kato and Takéuchi, 1983). (**a**) Projection onto the **ab** plane; the subcell, determined by the octahedral cations (stippled circles) only, is shaded. The supercell describing the entire structure is outlined. (**b**) View along [110].

Cu^{2+} silicates (Kawamura and Kawahara, 1977; Hefter and Kenney, 1982; Heinrich, 1983). In modulated layer silicates the apical spread leads to the inversion of some of the tetrahedra within otherwise continuous sheets.

Bementite was first mentioned by Strunz (1957) as having an X-ray powder diffraction pattern similar to the sheet silicates schallerite and antigorite. Kato (1963) described bementite with an orthorhombic unit cell with $a = 14.5$, $b = 17.5$, and $c = 4 \times 7.28 = 29$ Å, based on electron diffraction patterns. He interpreted the chemical analysis as giving the formula $Mn_5Si_4O_{10}(OH)_6$. Kato and Takéuchi (1980) revised this formula to $Mn_7Si_6O_{15}(OH)_8$ but used the earlier lattice constants for their structure suggestion in space group $P222_1$ with $Z = 16$. On the basis of the $hk0$ electron diffraction pattern, they suggested two hexagonal Mn sheets rotated relative to each other by 24°, linked by a tetrahedral sheet similar to that of pyrosmalite.

Eggleton and Guggenheim (1988) found that the pyrosmalite-like tetrahedral sheet failed to explain the alternating rotation of the octahedral sheet and that its size was inconsistent with the a and b dimensions of the unit cell of bementite. Using X-ray precession photographs and electron diffraction patterns, Eggleton and Guggenheim (1988) determined the unit cell to be monoclinic with $a = 14.83$, $b = 17.58$, $c = 14.70$, and $\beta = 95.5°$ and probable space group $P2_1/c$. Based on HRTEM images, they proposed a tetrahedral sheet, in which pairs of six-membered rings are connected by five- and seven-membered rings in such a way as to coordinate the oppositely rotated Mn sheets on either side of the tetrahedral sheet.

Table 1. Microprobe analyses in weight percent of oxides

Oxide	1	2	3	4	5
ZnO	2.36	2.18	2.42	2.31	2.44
FeO	6.40	6.24	6.33	6.24	6.42
MgO	3.29	3.22	3.29	3.13	3.11
MnO	39.00	39.02	38.96	39.00	38.97
Al_2O_3	0.09	0.09	0.08	0.14	0.17
SiO_2	39.42	39.28	39.12	38.24	38.44
Total	90.56	90.03	90.20	89.06	89.55

Note: analyses 1, 2, and 3 were taken on clear crystals, whereas analyses 4 and 5 were taken on fine-grained material from the core of the rosettes. The bulk density (including kutnahorite and amorphous material), determined by immersion is $\rho_{meas} = 3.085$ g/cm³.

This paper presents new electron diffraction data, HRTEM images, and powder X-ray diffraction data for bementite from Trotter mine, Franklin, New Jersey. Quantitative modeling of these data is used to determine both the parent structure and polytypism of bementite. A basic subcell model for the $^{[6]}$Mn sheet of bementite was first deduced from intensities and reflection positions of the $hk0$ electron diffraction pattern and resulted in a model similar to the one suggested by Kato and Takéuchi (1980). To relate the polytypism to the rather unusual features of the electron diffraction patterns, the approach for the description of interface modulations by Amelinckx et al. (1984) was used. Once the displacement vector was determined by relating HRTEM images to the subcell model, the stacking was deduced from the $h0l$ electron diffraction pattern. Possible models for the supercell were derived by considering stoichiometry, crystal chemistry, and symmetry. These were tested with distance least-squares (DLS) modeling. The preferred model, which has the topology proposed by Eggleton and Guggenheim (1988), was subsequently refined using Rietveld analysis of powder XRD data. Finally, the model was verified by comparing experimental HRTEM images with images calculated from the powder data model.

Sample

Bementite only occurs in heavily faulted small-grained crystals, the domains of which are not large enough to allow a single-crystal structure determination. The sample used in the present study is from the Trotter mine, Franklin, New Jersey (Australian Museum, Sydney; sample number = D26839). Bementite shows a prominent (001) cleavage and a secondary (010) cleavage. The brownish platy crystals form rosettes around an opaque core of very poorly crystallized material, which contains veinlets of kutnahorite, $Ca(Mn,Mg)(CO_3)_2$, and probably also some amorphous oxides. Wavelength-dispersive analysis with a Cameca Camebax electron microprobe (Table 1) gave an average mineral composition of $Zn_{0.23}Fe_{0.81}Mg_{0.74}Mn_{5.07}Al_{0.02}Si_{5.98}O_{15}(OH)_8$.

Experimental

High-resolution transmission electron microscopy: HRTEM

For the *hk*0 diffraction pattern a crushed-grain sample was used. The cleavage of bementite along the layers prevented the use of crushed-grain samples for the other directions; thus ion milling of a thin section was used instead. This method also has the advantage of avoiding deformation-induced stacking faults.

For experimental images and diffraction patterns a JEOL 200CX electron microscope operating at an accelerating voltage of 200 kV was used. For the experimental HRTEM images, an aperture diameter of 2.83 $Å^{-1}$ was chosen, which allowed beams with maximum values of $h = 20$, $k = 25$, and $l = 20$ to pass. Thus real space was sampled in 0.75-Å intervals.

During the diffraction experiments it was occasionally observed that the diffraction patterns from different areas of the same grain were oriented slightly differently, causing the center of the Laue zone to be shifted by approximately one to two reciprocal cell constants (≈1–2 milliradians) in a random direction. This suggests that the crystal flake under observation is slightly buckled. Hence the observed images might appear to have a lower symmetry than the projection of $P2_1/c$ onto the imaged plane implies. A slight deviation from centrosymmetry may also suggest tilting of the beam (Smith et al., 1983).

The bementite samples were, in comparison with other modulated layer silicates (e.g., antigorite: Otten, 1993), surprisingly stable under the electron beam. Damage to the crystals could only be observed after an exposure to the fully condensed beam of approximately 3 min. Typically three to five images of a through-focus series at a magnification of 810 000× could be obtained before beam damage became apparent. Preliminary adjustments and focusing were done with a beam as widely spread as possible. The fine adjustment for the image recording was done on the same grain, slightly off the area of interest, so that the latter was only exposed to maximum intensity for the recording of the images.

Image simulations were calculated according to the multislice method (Cowley and Moodie, 1957; Goodman and Moodie, 1974), as implemented in the EMS program package by Stadelmann (1987). Imaging constants appropriate for the experimental conditions at an accelerating voltage of 200 kV were assumed (spherical aberration = 1.2 mm, semiangle of beam convergence = 0.5–0.8 milliradians, half-width of focal spread = 5–7 nm. Scherzer focus for this microscope occurs at −63.5 nm. The defocus settings were varied in steps in unit cells of 5 nm from an over-focus of 40 nm to an under-focus of −150 nm. The crystal thickness was increased in steps from one unit cell to about 10 nm. It was found that, for a crystal thickness above approximately 10 nm, the effects of beam and crystal tilt made an interpretation of the fine structural detail impossible. For the phase-grating calculations, the chosen slice thickness in the beam direction never exceeded 2.5 Å, and enough beams were included to sample real space in approximately 1-Å intervals. Any decrease in slice thickness or increase in beam number did not significantly alter the intensities of the transmitted beams for a given sample thickness.

Powder XRD

The powder diffraction data were recorded on a Scintag Diffractometer for $10° \leq 2\theta \leq 60°$, using Cu$K\alpha$ radiation. Preferred particle orientation along the main cleavage surface is a severe problem that would cause the intensity of reflections with $l \neq 0$ to be enhanced, depending on the inclination of the diffracting plane toward (00*l*). To minimize this, the sample was scratched with a fine needle directly off the specimen onto a flat metal holder coated with a film of Apiezon grease. The pattern still shows some preferred orientation, but it is less severe than with conventional preparation methods.

For the interpretation of the powder diffraction data, the X-ray Rietveld analysis program of Baerlocher (1982) was applied. This program package is particularly suited to problems where the refinement of a high number of independent parameters is required. Because of the incorporation of a DLS procedure in the refinement, it allows interatomic distances from earlier experiments to be used as extra data. These initial constraints prevent convergence toward a false minimum during the early stages of refinement. As the refinement progresses, the weight of these distances, or soft restrictions, relative to the diffraction data is decreased, ideally to zero.

Results

Electron diffraction data

The *hk*0 diffraction pattern. The diffraction pattern (Fig. 2a) taken from a thin foil shows a rectangular grid with $a = a_{bem} = 14.8$ (±0.3) Å and $b = b_{bem} = 17.6$ (±0.4) Å. Superimposed on the rectangular grid are strong reflections at $d_1 = 2.81$ (±0.03) Å and $d_2 = 1.63$ (±0.02) Å. These can be attributed to two hexagonal nets with $a = 2.8$ Å, which are rotated by 22° relative to each other (Fig. 2b). For simplicity, all Miller indices are given on the basis of the bementite supercell. The first net is determined by the cell 000, 440, 920, and $5\bar{2}0$, the second net by the cell 000, 160, 680, and 520. The strong reflections alone can be indexed on the basis of a subcell with $a_{Mn} = a_{bem}$ and $b_{Mn} = b_{bem}/2$, which will be called the Mn subcell.

The *h*0*l* diffraction pattern. The diffraction patterns (Fig. 3) were from the same grain within approximately 100 nm of each other, near the wedge-shaped edge of the grain, thinned by ion milling. Hence the thickness of the sample is different for each diffraction pattern.

The main difference among the diffraction patterns in Figure 3 is the position of the diffracted spots and streaks. Figure 3a shows the *h*0*l* diffraction pattern expected for the net of ordered bementite. The spots can be attributed to a monoclinic net with $\beta^* = 84.5°$. Figure 3b–3e show

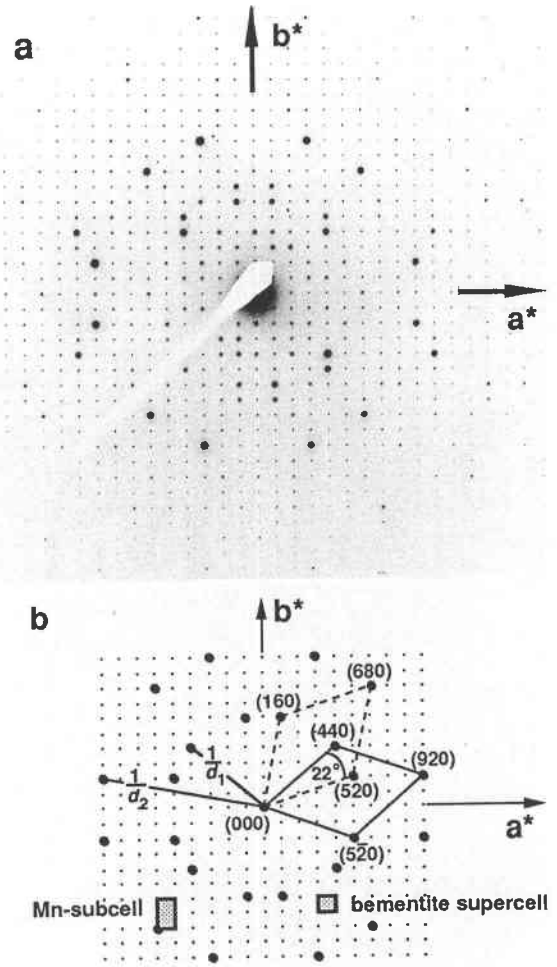

Fig. 2. The $hk0$ electron diffraction pattern of bementite; (**a**) experimental diffraction pattern; (**b**) explanatory sketch. The big black dots represent the reflections with $6h \pm k = 28n$ to which Mn contributes. They are arranged in circles around 000: one with radius $1/d_1$ with $d_1 = (\sqrt{3}/2)d_{(Mn\text{-}Mn)}$, the other with radius $1/d_2$, with $d_2 = \frac{1}{2}d_{(Mn\text{-}Mn)}$ (see also Fig. 10). Each of the two hexagonal cells, drawn with a solid or a dashed line, respectively, shows the unit cell of one of the two hexagonally based Mn sheets that are rotated against each other by 22°. Combining these two cells leads to the Mn subcell that extends over half the b dimension of the bementite supercell. All Miller indices are given on the basis of the bementite supercell.

diffraction patterns in which bands of reflections are shifted along **c***. These bands, each ranging over a limited extent of h values, mostly show the $l = 2n + 1$ absences, characteristic of ordered bementite. However, the β^* angles within these bands vary systematically as a result of the increasing frequency of stacking faults (Fig. 3). The $00l$ and $14{,}0{,}l$ reflections, the latter occurring at approximately 1 Å^{-1} from the central beam, are sharp and of comparatively high intensity. Very faint first-order Laue zone reflections are observed at the theoretically expected distance to the central beam of 2.1 Å^{-1}, where they form rings 0.1 Å^{-1} wide, i.e., the outermost zero-order Laue zone reflections are separated by a gap of approximately 1 Å^{-1} from the first-order Laue zone reflections. The rows between $00l$ and $14{,}0{,}l$ show streaking of a variable degree. The $h0l$ rows with $h = 4$ or 5 and $h = 9$ or 10 are less streaked along **c*** than the ones for the remaining h values. In Figure 3f, the bands disappear again in favor of a net with $\beta^* = 71°$. The bandlike appearance of the $h0l$ diffraction patterns and the variation in β^* can be interpreted with stacking disorder (discussion below).

Most $h0l$ diffraction patterns show only the reflections for which l is even, whereas Figure 3c–3e show a faint intensity, also for the kinematically forbidden l = odd reflections. For a perfect crystal, reflections that are kinematically forbidden because of a glide plane should be absent, even under dynamical diffraction conditions, if the incident beam is perpendicular to the glide plane, and if only zero-order Laue zone reflections have to be considered in the multiple scattering process (Gjønnes and Moodie, 1965). For a $h0l$ diffraction pattern from a crystal with space group $P2_1/c$, the incident beam is parallel to [010], that is, parallel to the 2_1 axis and perpendicular to the c glide plane. However, kinematically forbidden reflections may be introduced even by a thin crystal, if higher order Laue zone reflections are involved in the dynamical scattering process and the crystal is not perfectly oriented, or if the material is a faulted crystal, as represented by the diffraction pattern in Figure 3b–3e. In fact the l odd reflections are strongest in the diffraction pattern of the most faulted phase, Figure 3e.

The 0*kl* diffraction pattern. Most of the $0kl$ diffraction patterns show an interaxial angle of 90° but no systematic absences (Fig. 4). However, on a diffraction pattern taken from a thin foil, the $00l$ reflections with $l = 2n$ and the $0k0$ reflections with $k = 2n$ are of greater intensity than those with l or k odd.

Some of the $0kl$ diffraction patterns show minor but random deviations from the 90° interaxial angle, and in some the ideal 90° pattern is superimposed by a weak second diffraction pattern whose interaxial angle deviates slightly from 90°. This deviation from the ideal 90° angle is probably an orientation effect, but it could also suggest regularly occurring stacking faults, with a small shift component in the **b** direction, or triclinic symmetry for the parent structure. In contrast to the $h0l$ diffraction patterns, the $0kl$ diffraction patterns show no, or only very faint, streaking along **c***; most of the observable streaking is along **b***.

HRTEM images

The image of a projection along [010] (Fig. 5) was taken at a defocus setting of approximately −50 nm. The dark bands parallel to **a**, which occur every 7.4 Å in the **c** direction, are separated by lighter bands showing sets of three bright blobs forming triangles that alternate pointing up and pointing down. The triangles of the same orientation in subsequent bands are stacked to include an angle of 95.5° with the **a** axis. A [010] projection, taken

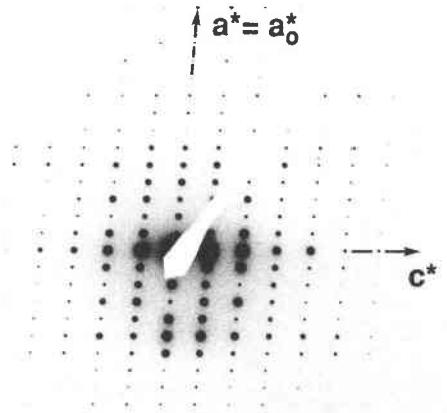

a) fault-free phase: Variety I
$\beta^* = \beta_o^* = 84.5°$ ($p \approx 50$)

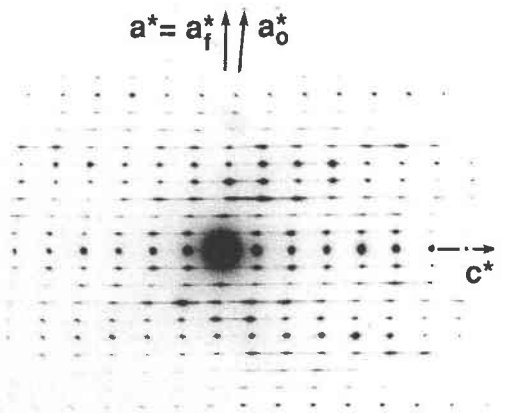

b) fault every 5th Mn-layer:
$\beta^* = \beta_f^* = 90°$ ($p = 5/2$)

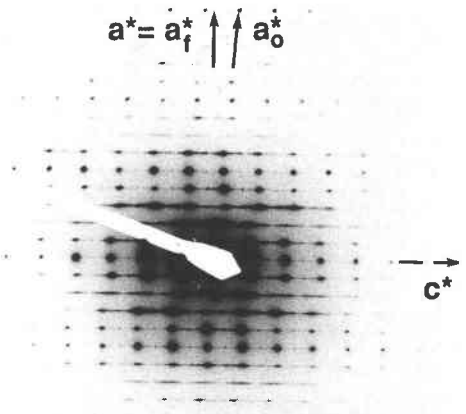

c) fault every 4th Mn-layer:
$\beta^* = \beta_f^* = 91°$ ($p = 4/2$)

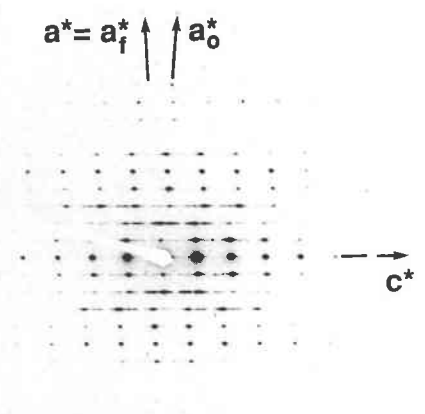

d) fault every 3rd Mn-layer:
$\beta^* = \beta_f^* = 93°$ ($p = 3/2$)

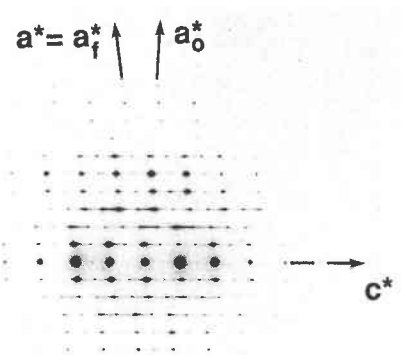

e) fault every 2nd Mn-layer:
$\beta^* = \beta_f^* = 97°$ ($p = 2/2$)

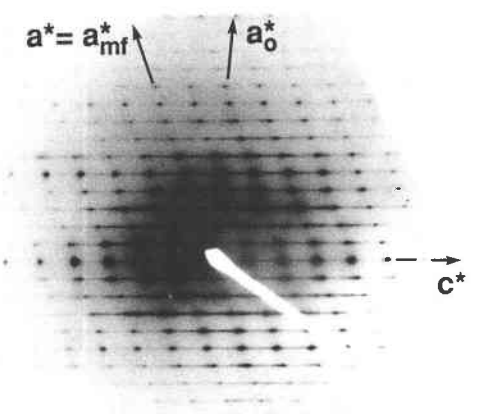

f) fault every Mn-layer: Variety II
$\beta^* = \beta_{mf}^* = 71°$ ($p = 1/2$)

Fig. 3. The *h*0*l* electron diffraction patterns of bementite. The *h*0*l* diffraction patterns show the variation in average stacking fault abundance between the parent phase of bementite, Variety I (**a**), and maximally faulted bementite, Variety II (**f**). Both varieties have a monoclinic *h*0*l* grid, Variety I with $\beta^* = \beta_o^* = 84.5°$ and Variety II with $\beta^* = \beta_{mf}^* = 71°$. Intermediate phases (**b–e**) have bands of reflections shifted along **c***. The vector $\mathbf{a}_o^*$ marks the reciprocal lattice vector of the ordered Variety I in all of the *h*0*l* diffraction patterns. For fully ordered bementite, $\mathbf{a}_o^* = \mathbf{a}^*$. The variable vector $\mathbf{a}_f^*$ gives the reciprocal lattice vector **a***, predicted for intermediate stacking fault densities (**b–e**) characterized by *p*, the distance between faults measured in unit cells. For the maximally faulted phase (**f**), $\mathbf{a}^* = \mathbf{a}_{mf}^*$.

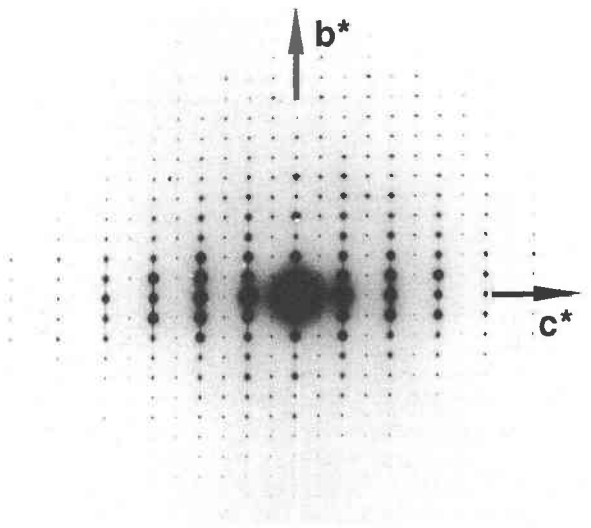

Fig. 4. The $0kl$ diffraction pattern. Note the very slight streaking along **b***, suggesting an irregularity in the **b** repeat (cf. Fig. 7).

near the Scherzer focus, of a bementite with a high degree of stacking disorder (Fig. 6a) shows similar inverting triangles, but here the 95.5° angle to the **a** axis is maintained over a maximum of 1.5 *c*-cell constants only. The stacking faults occur on average after one unit-cell repeat in the **c** direction. To eliminate doubts about the origin of the spot shifts in the $h0l$ diffraction patterns (Fig. 3b–3f), a laser optical diffraction pattern (Fig. 6b) of the negative of the HRTEM image in Figure 6a was taken. Because the diffraction pattern averages the crystal structure over approximately 200 times the area imaged in a HRTEM image [selected-area electron diffraction (SAED) aperture = 20 μm, magnification for HRTEM image = 550 000×] the observed diffraction pattern is only characteristic of the imaged area if the average amount of faults within the imaged area is representative of the whole area from which the diffraction pattern is taken. The resulting laser optical diffraction pattern (Fig. 6b) is virtually identical to the electron diffraction pattern in Figure 3e.

The triangles pointing down in the HRTEM image of Figure 5 are faintly connected by a brighter fringe. This fringe becomes more intense with increasing specimen

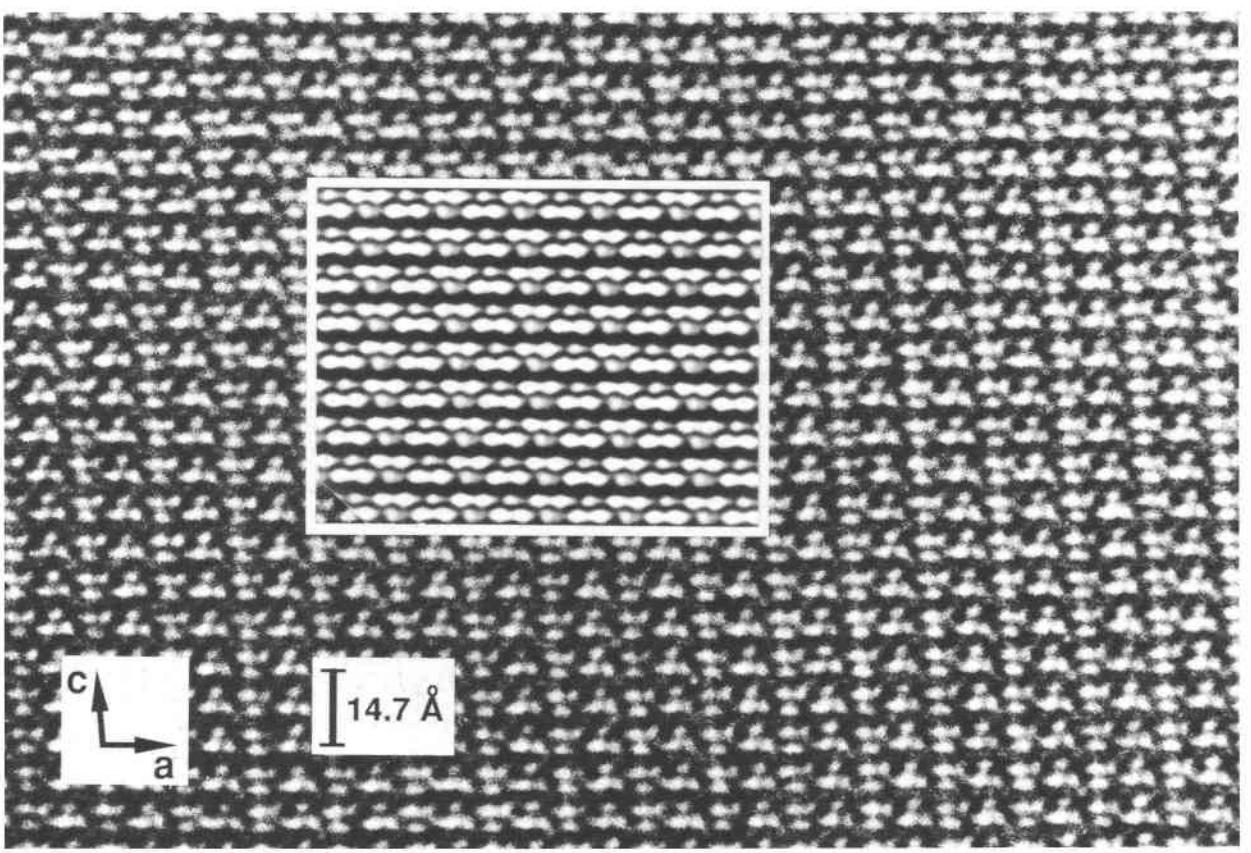

Fig. 5. Match between representative experimental and calculated images of a projection along [010] at a defocus setting of −50 nm, close to Scherzer focus of −63.5 nm. Experimental and simulated images (inset) have the same dark bands for the Mn layers, separated by lighter bands for the tetrahedral layers, showing sets of three bright blobs in triangles that invert alternately.

thickness but is nearly nonexistent at the very edge of the grain.

Figure 7 shows projections along [100] at defocus settings of +10 and −15 nm, respectively. The appearance of this projection seems to be particularly susceptible to minor variations in crystal or beam tilt. Bright continuous wavy lines spaced at 7.4-Å intervals separate dark bands, which have a bright dotted line of the same wavelength *b* but with a greater amplitude weaving through it. In Figure 7b the dotted line shows four dots per unit-cell repeat *b*. Dark areas are arranged alternately on either side of the light dotted line. At the right side of the image, the periodicity of the structure is disturbed, showing an area where the wavelength is approximately doubled.

The HRTEM image of the [110] projection, taken close to Scherzer focus, (Fig. 8a) shows rows of dark elongated blobs 2.8 Å apart. These dark rows are separated by brighter, spotty bands 14.7 Å wide, which themselves are divided by a darker line. Figure 8b shows an overview of the [110] projection. Here the dark rows are separated by 1, 2, or 3 times *c*, but never by *nc*/2.

Powder X-ray diffraction pattern

The three strongest lines in the powder pattern of bementite (Fig. 9) are indexed as d_{002} = 7.321 (intensity = 100), d_{004} = 3.658 (intensity = 23), and d_{014} = 3.582 Å (intensity = 50). The intensity of 014 is 2.2 times greater than the intensity of 004, a ratio which is unusual for a normal sheet silicate. The 00*l* lines are narrower then the remaining *hkl* lines.

The pattern used for the profile analysis shows kutnahorite lines of low intensity, with the highest peak at *d* = 3.025 Å, and the line at *d* = 2.96 Å, also questioned by Guggenheim and Eggleton (1988), is observed as a very broad peak of low intensity. Neither line was found in Gandolfi patterns of the relatively coarse-grained material used in this study. The line at 2.96 Å corresponds with the 220 line expected from a spinel structure, in which it represents the nearest distance between octahedral cations. Hence it could mark the distance between cations in the amorphous material contained in the poorly crystallized center of the bementite rosettes. A small rise in the background of the diffraction data between $2\theta \approx 30$ and 40° also indicates the presence of amorphous oxides (Cruz and Real, 1991).

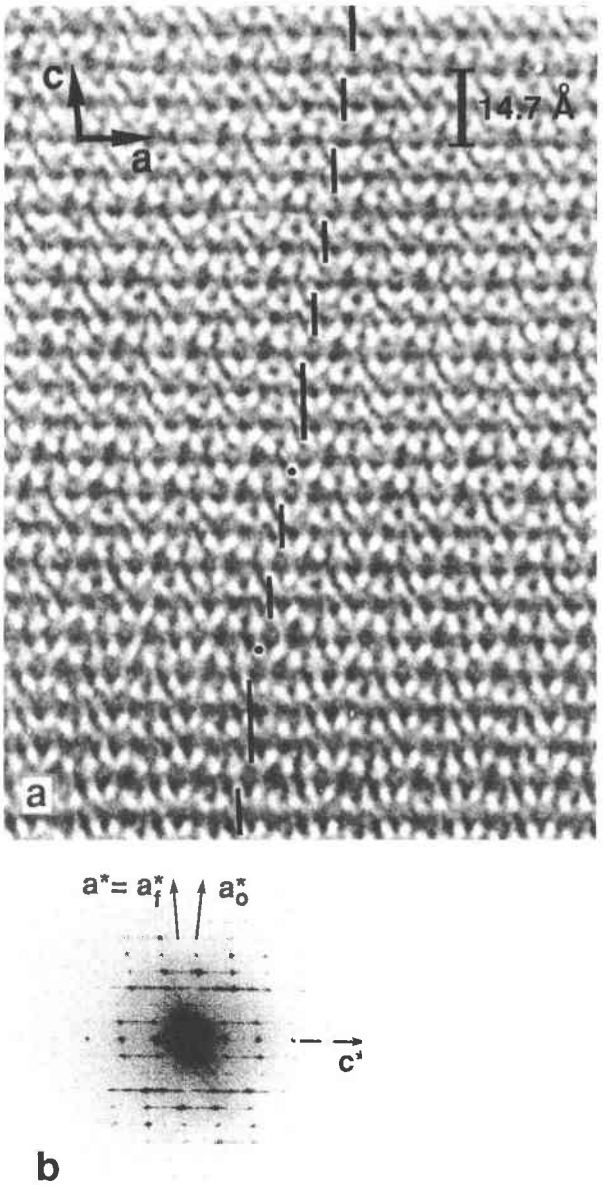

Fig. 6. (**a**) HRTEM image of faulted bementite projected along [010]. The stacking errors are indicated with the dotted and dashed line and occur, on average, after every second Mn layer. (**b**) Laser-optical diffraction pattern of the negative of the HRTEM image in **a**. In this diffraction pattern, $\beta^* = 97°$ (angle between $\mathbf{a}_f^*$ and $\mathbf{c}^*$), as in the electron diffraction pattern of Fig. 3e.

Derivation of the subcell model

The *hk*0 diffraction pattern (Fig. 2) shows a number of reflections at d_1 = 2.81 and d_2 = 1.63 Å, which are clearly stronger than the rest. These can be attributed to two hexagonal nets that are rotated by 22° relative to each other. On the basis of the bementite cell the reflections in the first net have indices 440, $\bar{1}60$, $\bar{5}20$, 920, 3,10,0, $\bar{6}80$, plus centrosymmetric reflections. The reflections in the second net have indices $\bar{4}40$, 160, 520, $\bar{9}20$, $\bar{3}$,10,0, 680, plus centrosymmetric reflections. The relatively high intensities of these reflections indicate that they are caused by lattice planes of high Mn content. In agreement with the HRTEM images (Figs. 5, 7, and 8), which show no interruption in the Mn sheet, it was assumed that bementite contains continuous hexagonal trioctahedral sheets of Mn approximately parallel to the **ab** plane. Thus, we suggest that the first net represents an Mn sheet with the most densely occupied rows along [610], [250], and [1$\bar{1}$0], and the second net represents an Mn sheet with rows along [6$\bar{1}$0], [2$\bar{5}$0], and [110] (Fig. 10). This is in

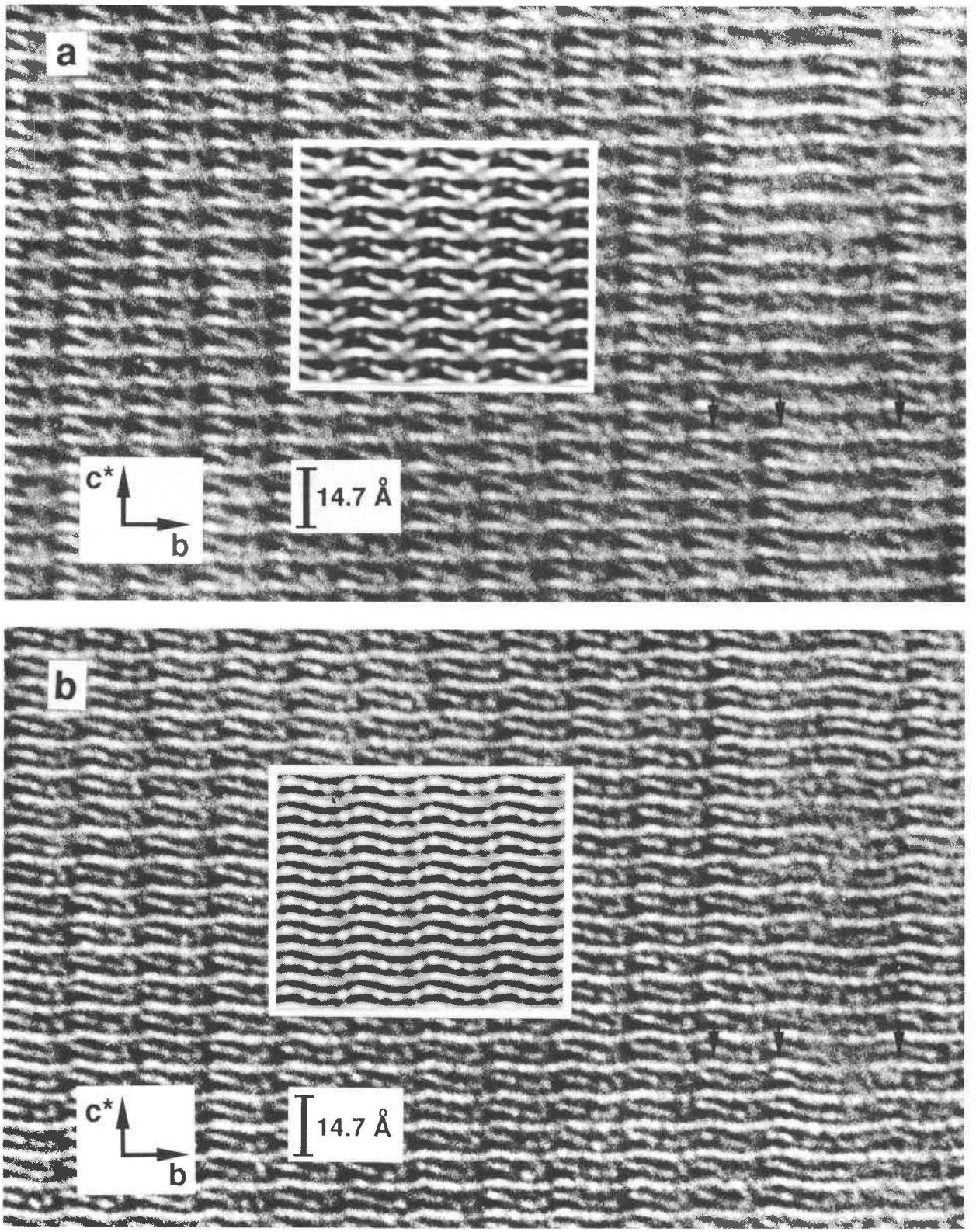

Fig. 7. Comparison between two representative experimental and calculated images of a projection along [100], at defocus settings of +10 (**a**) and −15 nm (**b**). The images resemble negatives of a Scherzer-focus image. Continuous bright wavy lines show the corrugated Mn layers; bright dotted lines represent the tetrahedral sheet (best distinguished in **b**). The best match for the simulated images (inset) were obtained if the center of the Laue zone was shifted to $02\bar{1}$, indicating a slight tilt of the sample. Along the right side of the images is an area, marked by arrows, with approximately doubled **b**-axis repeat, consistent with the slight streaking along **b*** in the $0kl$ diffraction pattern (Fig. 4).

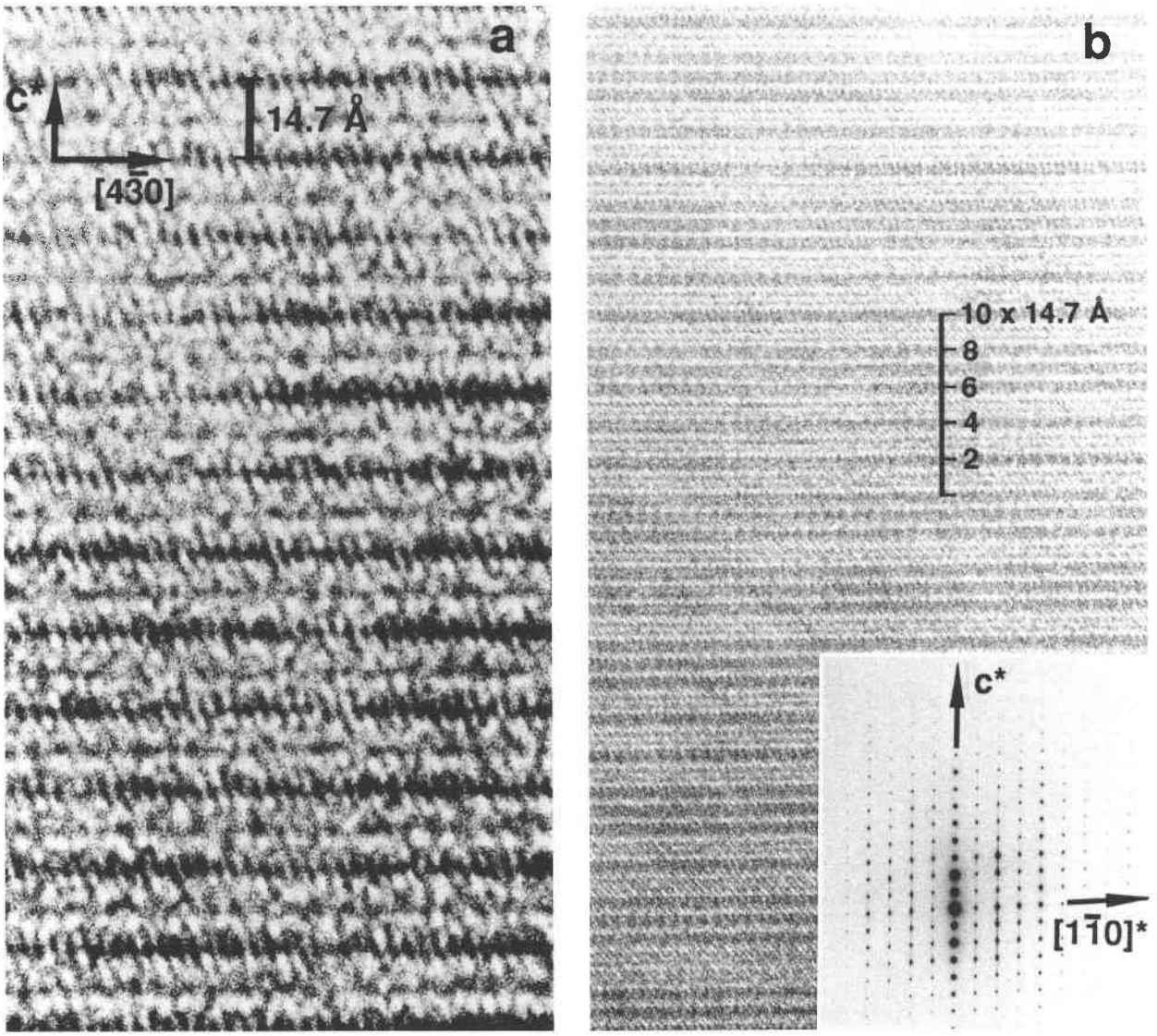

Fig. 8. Experimental images projected along [110], close to the Scherzer focus. (**a**) Conspicuous dark bands resolve slightly elongate blobs, 2.8 Å apart ($=d_1$ in Fig. 10), representing the most densely occupied rows of Mn aligned parallel to the beam in [110] projection. Alternating Mn layers, which do not have their rows aligned with respect to the beam, show much less contrast and appear as faint dark bands. (**b**) Overview of the [110] projection. The high contrast Mn layers are separated by 1, 2, or 3 times the c-axis repeat of 14.7 Å, but never by $nc/2$, indicating that adjacent Mn layers are always rotated against each other. Inset: [110] electron diffraction pattern.

agreement with the observation in the HRTEM image of a [110] projection (Fig. 8a) where the Mn rows with distances d_1 = 2.8 Å are aligned with the beam in every alternate Mn sheet only, at 14.7-Å intervals. The d values, i.e., the distances between the lattice planes, are consistent with an average Mn-Mn distance of 3.25 Å, with $d_1 = (\sqrt{3}/2)d_{(\text{Mn-Mn})}$ and $d_2 = \frac{1}{2}d_{(\text{Mn-Mn})}$ (see Fig. 10).

The c-axis repeat of 14.7 Å allows for two Mn sheets parallel to (001). The direction of the most densely occupied rows suggests that they are rotated alternately by either plus or minus 22°/2 from **a** (Fig. 10). The space group with maximum symmetry that allows for two rotated Mn sheets is $P2_1/c$. To obey the symmetry requirements, the two sheets must be at $z \approx 0$ and $z \approx \frac{1}{2}$, with one Mn atom positioned on the center of symmetry at the origin of the unit cell. With the a and b dimensions of the Mn subcell (see Figs. 2b and 10), the Mn-Mn distance, and the direction of the most densely populated Mn rows, the Mn coordinates in the subcell can be determined for the two sheets as $(3m/14, m/14, \approx 0)$ and $(3m/14, -m/14, \approx \frac{1}{2})$, respectively, with m equal to an integer between 0 and 14. Hence, Mn contributes only to subcell reflections with $3h \pm k = 14n$.

In the full bementite supercell, which extends over two

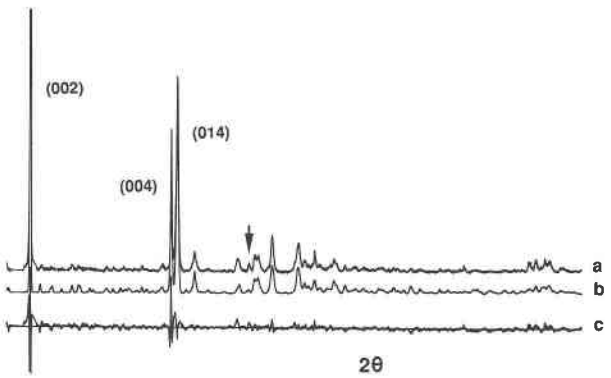

Fig. 9. Measured (a) and calculated (b) powder X-ray diffraction pattern, and their difference (c). The peak of the amorphous oxides is marked with an arrow. The 002 reflection has been truncated to show the less intense reflections in more detail. The 2θ range is from 10 to 60°.

Mn subcells in the **b**-axis direction (Fig. 10), Mn contributes to reflections with $6h \pm k = 28n$, and the position of the Mn can be given as $(6m/28, m/28, \approx 0)$ and $(6m/28, -m/28, \approx \frac{1}{2})$, with m equal to an integer between 0 and 28.

Stacking faults and polytypism

The polytypism of bementite can be described by lateral displacements of essentially identical tetrahedral sheets whose internal topology does not affect the description of the stacking faults. The displacement of slabs parallel to the Mn layers, most evident in a projection along [010], can easily be characterized with the knowledge of the subcell alone. Figure 6a shows a heavily faulted area in which a shift occurs after every second Mn layer, on average.

The projection of the shift on **a** is approximately $\frac{1}{8}a$. By comparison with the subcell model (Mn sheets only, Fig. 10) this observation suggests a displacement of the tetrahedral sheet from the unfaulted stacking sequence by one Mn-Mn distance along [610] or [6$\bar{1}$0]. Displacements along [250], [2$\bar{5}$0], [110], and [1$\bar{1}$0], which have a shorter projection on **a**, were not observed in any of the images projected along [010]. Therefore the displacement vector **R**, which lies in the **ab** plane, was assumed to be $\frac{1}{28}(6\mathbf{a} \pm \mathbf{b})$, which is the vector between two nearest Mn atoms along [610] or [6$\bar{1}$0], respectively (Fig. 10).

The reflections in the $h0l$ patterns are sharp wherever the displacement vector $\mathbf{R} = \frac{1}{28}(6\mathbf{a} \pm \mathbf{b})$ multiplied by the diffraction vector $\mathbf{g} = h\mathbf{a}^* + k\mathbf{b}^* + l\mathbf{c}^*$ is an integer, i.e., if **R** is a lattice vector. This only holds for $h = 14$, and Figure 3 indeed shows that the reflections in the 14,0,l row are sharp. For reflections in the rows $h = 5$ ($\mathbf{g}\cdot\mathbf{R} = 1.07$ and $h = 9$ ($\mathbf{g}\cdot\mathbf{R} = 1.93$), $\mathbf{g}\cdot\mathbf{R}$ is close to an integer and, as expected, the reflections within these rows are sharper than the ones in the remaining rows.

In some diffraction patterns only the sharper rows are detectable. Because the tetrahedral sheets are isolated between adjacent rigid octahedral sheets, it is assumed, as a first approximation, that the stacking fault does not induce structural changes in the tetrahedral sheet. Thus, one stacking fault changes the intensity expression by a phase factor of $\cos(2\pi\mathbf{g}\cdot\mathbf{R})$, so that $I_{h0l} = 2F^2_{h0l}[1 + \cos(2\pi\mathbf{g}\cdot\mathbf{R})]$. The reflections are weaker for $\mathbf{g}\cdot\mathbf{R} \neq m$, where m is an integer, and extinguished for $\mathbf{g}\cdot\mathbf{R} = m/2$. Indeed, the reflections in the rows with $h = 5$, 9, and 14 ($\mathbf{g}\cdot\mathbf{R} = 1.07$, 1.93, and 3.00) are of higher intensity, whereas the reflections in the rows with $h = 2$, 7, and 12 ($\mathbf{g}\cdot\mathbf{R} = 0.43$, 1.50, and 2.57) are considerably weaker, thereby enhancing the bandlike characteristic of the $h0l$ diffraction patterns of the intermediate phases (Fig. 3b–3e). In particular, the row with $h = 7$ ($\mathbf{g}\cdot\mathbf{R} = 1.50$) nearly vanishes in the $h0l$ diffraction pattern of the intermediate phases.

The periodic introduction of parallel planar translation interfaces, such as stacking faults with a displacement vector **R**, produces satellite spots. The direction of the arrays of satellites is parallel with the unit normal $\mathbf{e}_n$ on the interface. The spacing between satellite spots is determined by the average spacing between interfaces, d, (Megaw, 1960). The diffraction vector of the defaulted phase, $\mathbf{g}_{sf}$, is given in terms of the diffraction vector of the parent structure, **g**, by (Amelinckx et al., 1984; Van Landuyt, 1991): $\mathbf{g}_{sf} = \mathbf{g} + (n + \mathbf{g}\cdot\mathbf{R})\mathbf{e}_n/d$ with n = order of the satellite = 0, ±1, ±2. . . . For an $h0l$ diffraction pattern, in which the effects of the stacking faults can be seen most clearly, the location of the diffraction spots of the faulted structure can be found by substituting $\mathbf{R} = 3\mathbf{a}/14$, $\mathbf{e}_n = \mathbf{c}^*/|\mathbf{c}^*|$ and the spacing between stacking faults measured in unit cells, $p = d\cdot|\mathbf{c}^*|$ in the above formula: $\mathbf{g}_{sf} = \mathbf{g} + (n + \mathbf{g}\cdot\mathbf{R})\mathbf{c}^*/p = h\mathbf{a}^* + [l + (n + 3h/14)/p]\mathbf{c}^*$.

The zero-order diffraction spots ($n = 0$) in the expression describe a pattern with the β^* angle of the faulted variety, the satellites of which would be found at intervals $n|\mathbf{c}^*|/p$ along $\mathbf{c}^*$. In the case of bementite, it may be expected that only the reflections around the parent structure spots with $\mathbf{g}\cdot\mathbf{R} = 1$ are of sufficient intensity to be visible. This qualitatively explains the bandlike appearance of the $h0l$ diffraction patterns. Further verification would require detailed structure-factor calculation, because the approximation for the relative intensities by Van Landuyt (1991) only holds for interface modulations at an average distance of several unit cells.

For a known displacement vector **R**, the average spacing between stacking faults, p, is determined by the displacement of the spots in the faulted pattern from the position of the spots in the parent pattern. The value p can readily be found for zero-order spots ($n = 0$) in the row $h = 14$, for which $\mathbf{g}_{sf}$ reduces to $\mathbf{g}_{sf} = 14\mathbf{a}^* + l\mathbf{c}^* + 3\mathbf{c}^*/p$. The first two terms in this expression give the location of the spot for the parent phase, whereas $3/p$ in the last term gives the shift along $\mathbf{c}^*$. The observed shift in the 14,0,l row in the laser optical diffraction pattern (Fig. 6b), as in the similar diffraction pattern of Figure 3e, is

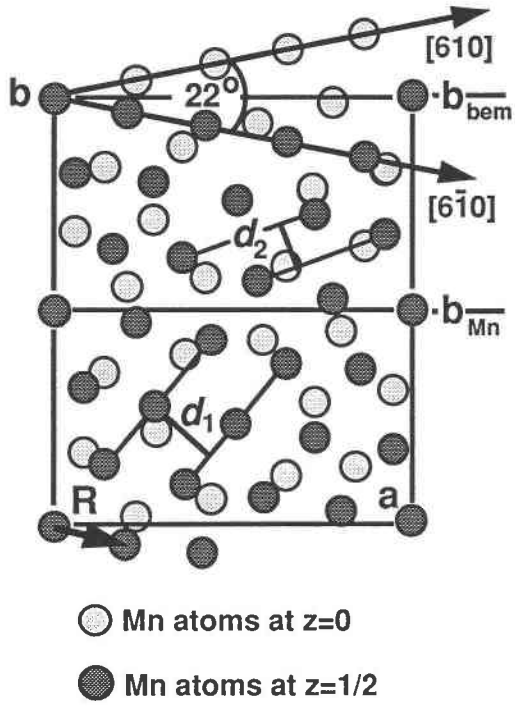

Fig. 10. Projection of the two rotated Mn sheets onto the **ab** plane. The Mn rows of the top layer at $z \approx ½$ (darker circles) are rotated by 22° relative to the Mn rows of the bottom layer at $z \approx 0$ (lighter circles). The most densely occupied Mn rows run along [110], [6$\bar{1}$0], [2$\bar{5}$0] for the top layer and [1$\bar{1}$0], [610], [250] for the bottom layer. The relation $d_1 = (\sqrt{3}/2)d_{(Mn\text{-}Mn)} = 2.81$ Å gives the distance between the ($\bar{4}$40) stack of lattice planes, whereas $d_2 = ½d_{(Mn\text{-}Mn)} = 1.63$ Å is the distance between the (680) stack of lattice planes. The vector **R** (bottom left corner) shows the displacement of the tetrahedral sheet by a stacking fault.

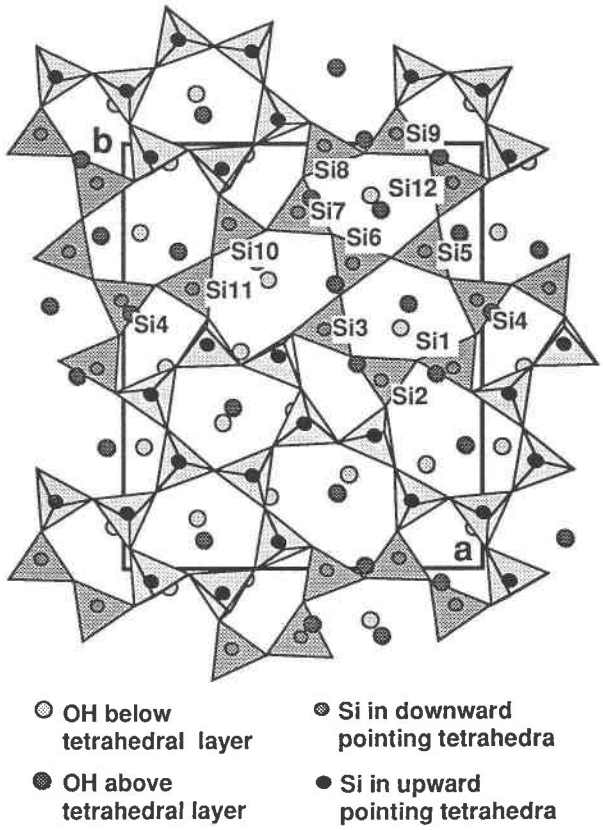

Fig. 11. Projection of the tetrahedral sheet at $z \approx ¼$ onto the **ab** plane. The tetrahedra pointing upward are shaded lighter than the ones pointing down. Only the Si atoms of the asymmetric unit are labeled. This tetrahedral sheet is sandwiched between the two Mn layers shown in Fig. 10. Also shown are the OH groups above and below the pictured tetrahedral sheet, which, together with the apical O atoms, form a hexagonal close-packed layer.

3**c***, and hence $^3/_p = 3$ and $p = 1$. Indeed, the average spacing between stacking faults in the corresponding HRTEM image (Fig. 6a, vertical bars) is one unit cell. Figure 3b–3f have the spots in the 14,0,l row shifted by $^6/_5$, $^3/_2$, 2, 3, and 6 times **c***, respectively. Hence they represent stacking varieties with faults after $^5/_2$, $^4/_2$, $^3/_2$, $^2/_2$, and ½ unit-cell repeats (i.e., after five, four, three, two, and one Mn layers, as one unit cell contains two Mn layers).

The suggestion of Kato (1963) for a unit cell with a c repeat of 28 Å may thus describe an intermediate stacking variety with a shift after every fourth Mn layer and $\beta = 89.3°$, such as the one represented by the diffraction pattern shown in Figure 3c.

In summary, bementite from Franklin can be described as a mixture of two stacking varieties: Variety I, which has no stacking faults and $\beta = 95.5°$, represented by the diffraction pattern in Figure 3a; and Variety II, which has a stacking fault at every Mn layer and $\beta = 71.3°$, as represented by the diffraction pattern in Figure 3f.

Derivation of the supercell model

The symmetry and analyzed mineral composition permit only two supercell models that are compatible with the space-group information, one of which can be excluded on the basis of the intensity data of the powder XRD pattern. The remaining model is shown in Figure 11.

Symmetry

The full bementite supercell extends over two Mn subcells in the **b**-axis direction (Figs. 2b, 10) because of the periodic reversal of tetrahedral apices (i.e., the modulation of the tetrahedral sheet with a wavelength of $2b_{Mn}$). The possible space groups with maximum symmetry for the supercell, if one considers only the subcell cations, is either $P2/c$ or $P2_1/c$. Based on the quality of the available data, it is not reasonable to reduce the symmetry further than strictly necessary, even though the minor deviation

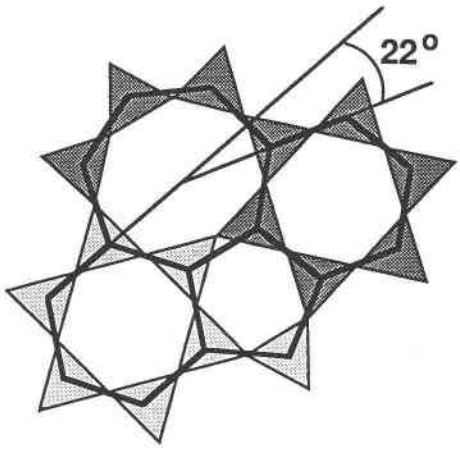

Fig. 12. Building principle of the tetrahedral sheet in bementite. The two six-membered rings with tetrahedra pointing in opposite directions (shaded differently) are connected by a five- and a seven-membered ring to impose alternate rotation by 22° onto the adjacent Mn layers.

from the 90° angle in the $0kl$ diffraction pattern (Fig. 4) could be interpreted as evidence for lower symmetry.

Because of the dynamical effects in a mosaic crystal, the TEM diffraction patterns do not restrict the choice of space group, and the data from precession photographs were of insufficient quality. However, the HRTEM image of a projection along [100] (Fig. 7) shows a glide plane rather than a mirror plane parallel to the Mn layers, visible as bright wavy lines. This is consistent with $P2_1/c$, but not with $P2/c$.

Topology of the tetrahedral sheet

With the assumption that Zn, Fe, Mg, and Mn are in octahedral coordination, the chemical analysis shows a ratio of octahedral to tetrahedral cations of 1.15 (±0.02). For a structure with continuous octahedral sheets, the unit cell requires 56 octahedral cations and hence 48.7 (±0.8) tetrahedral cations. To conform with the space group $P2_1/c$, the unit cell can contain either 48 tetrahedral cations placed on 12 general positions, or 50 tetrahedral cations placed on 12 general positions plus one special position. With the quality of the crystals and the error of the analysis, plus the fact that the special positions on the centers of symmetry are already taken up by Mn, it seemed reasonable to assume 48 tetrahedral cations per unit cell, that is, 12 tetrahedra in the asymmetric unit. To accommodate 49 tetrahedral cations, the symmetry of the structure would need to be reduced.

The unit-cell repeat of roughly 2 × 7 Å perpendicular to the layers suggests a single tetrahedral sheet at $z \approx 1/4$ containing tetrahedra with apices pointing in both (positive and negative) **c**-axis directions. The 2_1 axis along **b** at $z \approx 1/4$ requires equal numbers of tetrahedral apices in both directions.

Observed and calculated HRTEM images of projections along [100] (Fig. 7) are similar to those for the Scherzer focus, except that the contrast is reversed so that Mn layers (continuous lines) and tetrahedral sheets (dotted lines) appear bright in Figure 7. Thus the dark areas arranged alternately on either side of the tetrahedral sheet are interpreted as tunnels of low electron density running along **a**. Hence most apices of the tetrahedra adjacent to the tunnels are expected to point away from the tunnel, to coordinate with the adjacent Mn layer. None of the HRTEM images (Figs. 5, 7, 8) gives evidence for a discontinuous tetrahedral sheet.

The tetrahedral sheet of most layer silicates has the six-membered ring as their basic building unit. The rotation of the Mn sheets above and below the tetrahedral sheet by 22° requires that these six-membered rings, alternately pointing up or down, must be connected through single five-membered rings that share edges with the six-membered rings (Fig. 12). The ideal five-membered ring rotates the six-membered rings on opposite sides by 24° relative to each other. This angle is reduced by the strain of a seven-membered ring, which also connects the two six-membered rings sharing one edge with the five-membered ring. Connection by means of a seven-membered ring alone would rotate the six-membered rings by 17° only.

To contain the appropriate number of tetrahedra, the asymmetric unit must consist either of two isolated six-membered rings, or of two edge-sharing six-membered rings connected by two extra tetrahedra. The former possibility can be excluded, since it is not possible to join single six-membered rings with single five-membered rings to form a continuous tetrahedral sheet without the addition or subtraction of tetrahedra.

To coordinate the six-membered rings to the Mn sheets, the edges of the six-membered rings must include angles of $(\pm 11° + n \cdot 120°)$ with the orthohexagonal **a** axis, such that the longest extension of the double six-membered ring of the asymmetric unit is along either [250] (model A) or [610] (model B). Only two models are thus compatible with symmetry and lateral dimensions. Both models A and B have been refined with the DLS procedure of Baerlocher et al. (1976) to a R_D value of 0.030 and 0.027, respectively. The calculated powder pattern of model B with the longest extension of the double six-membered rings along [610] shows an intensity for the 011 reflection comparable with the intensity for the 014 reflection, and yet no 011 peak was observed in the bementite powder pattern. The minor contribution of the Si tetrahedral sheet to the $l = 2n + 1$ reflections in the $0kl$ diffraction pattern of a thin foil, where kinematical diffraction conditions are approached, suggests a quasi glide plane parallel to the (100) plane with a glide component $c/2$. This restriction only complies with model A, which has the longest extension of the double six-membered ring along [250], as shown in Figure 11. Thus only model A, which has the topology proposed by Eggleton and Guggenheim (1988), was considered further.

The DLS refinement showed that, in order to accommodate the tetrahedral sheet, the Mn sheet has to be corrugated with wave crests parallel to **a** and an amplitude of approximately $0.035 \times c$, i.e., an amplitude of 0.52 Å. The wavelike characteristic of the Mn sheet also explains the intensity ratio of 004 and 014 qualitatively. If one assumes the Mn sheet to be waved by a sinusoidal wave with amplitude A, so that $z_m = A \sin(2\pi y_m)$, calculation of the structure factors F (considering Mn only) shows F_{004} to be maximal for a flat Mn sheet ($A = 0$) and to decrease with increasing A. F_{014} is zero for $A = 0$ and decreases with A to a minimum at $A = 0.073 \times c$. Hence the intensity of the 014 reflection is maximal for a wave with an amplitude of 1.07 Å.

Powder pattern analysis

The X-ray Rietveld system by Baerlocher (1982) does not permit the simultaneous refinement of two phases. Hence the XRD pattern for the impurity phase kutnahorite (Frondel and Baur, 1955) was subtracted from the observed pattern of bementite by normalizing the kutnahorite pattern to its strongest peak at $d = 3.025$ Å. All bementite peaks overlapping this kutnahorite peak have calculated intensities below the standard deviation of the measurements.

A rise in the background between 30 and 40° 2θ, presumably originating from traces of amorphous oxides, could not be removed by automatic background correction, and the background was determined manually. Points of lowest intensity were measured, quadratically interpolated, and subtracted from the experimental profile. The values of 2θ were linearly corrected to agree initially with the values previously determined by Guggenheim and Eggleton (1988) and subsequently refined. Because of the stacking disorder, general hkl reflections are broader than the $00l$ reflections. To allow partly for the broadening of the general reflections in comparison with the $00l$ reflections, peak width and asymmetry were modeled with two experimental peak-shape functions (Hepp and Baerlocher, 1988). Despite a slight overlap, the peak-shape functions were determined from 004 at $2\theta = 24.31°$ for $00l$ reflections, and 014 at $2\theta = 24.85°$ for reflections with $h,k \neq 0$. Other peaks were unsuitable because they are composed of several overlapping reflections of approximately the same intensity. Using these peak-shape functions, the entire profile was analyzed for the dependence of peak width and asymmetry on 2θ.

The DLS-refined model A, with the longest extension of the double six-membered rings along [250], was used as input for the Rietveld procedure. A few DLS cycles lowered R_D to 0.011. Atomic scattering factors for neutral atoms were applied (Ibers and Hamilton, 1974). First the scale factor, preferred-orientation factor, and overall temperature factor were refined in separate blocks to avoid the effects of high mutual correlation. The overall temperature factor refined to 0.03 Å^2. To determine the preferred-orientation factor (POF), the function $\exp(\text{POF} \cos 2\delta)$, with δ being the angle between the preferred-orientation vector and the scattering vector, was refined to a POF value of 0.75. This yielded an R_{wp} of 0.37 and R_F of 0.17. The relatively low initial value for R_F suggests that the chosen topology for the tetrahedral sheet provides a good starting model. Half-width and peak asymmetry of the reflections with $h,k \neq 0$ were refined in four groups, depending on the angle between the diffraction vector of the particular reflection and the displacement vector **R**, to allow partly for the peak broadening due to stacking errors. Refinement of the z coordinates of Mn, as well as all the profile parameters, i.e., lattice constants, half-width, peak-asymmetry, and 2θ correction, lowered R_{wp} to 0.31 and increased the wave amplitude from the DLS value of $0.035 \times c$ to $0.050 \times c$. At this stage the Si atoms and the basal O atoms were removed from the model, and a difference-Fourier map was calculated. Thus, the phases were determined by the corrugated octahedral sheet only. The difference-Fourier map showed strong peaks for Si4, Si5, Si6, Si7, Si10, and Si11. For Si1, Si2, Si3, Si8, Si9, and Si12 the peaks were less obvious. Once the Si positions resulting from the strong peaks are established, there is no plausible alternative for a continuous tetrahedral sheet. Therefore the full model was introduced and refined, gradually decreasing the weight of the distance or soft restrictions relative to the intensity data from an initial 50 to a final 5%. The resulting atomic coordinates are listed in Table 2, and projections of parts of the structure are shown in Figures 10, 11, and 13. Observed and calculated patterns, as well as their differences are shown in Figure 9, and the parameters relevant for the Rietveld refinement are listed in Table 3.

The final difference-Fourier map showed, apart from ripples due to Mn, peaks of approximately 1.5–2 electrons at the positions of those Si atoms that superimpose after a stacking fault, i.e., at all Si positions except those of Si3 and Si12.

As the R_{wp} of 0.23 shows, the Rietveld refinement of the parent structure was only possible to a limited extent. One reason is the preferred orientation, which could not be completely eliminated in the experiment and only approximately modeled during the refinement. The other, and probably more important, restriction of the powder refinement is the abundance of stacking faults in the bulk sample. HRTEM images of ordered crystal domains between stacking faults were therefore used to test further the validity of the structural model.

HRTEM: Comparison between simulations and experimental images

The [010] projection

The image of a projection along [010] (Fig. 5), taken at a defocus of −50 nm, is close enough to the Scherzer focus (−63.5 nm) to give a true projection of the electron distribution of the structure, so that dark areas represent

TABLE 2. Atomic coordinates of the asymmetric unit

Atom	x	y	z	Atom	x	y	z
Si1	0.921	0.467	0.199	Si2	0.719	0.451	0.208
Si3	0.556	0.564	0.184	Si4	0.990	0.626	0.170
Si5	0.845	0.744	0.149	Si6	0.640	0.730	0.164
Si7	0.494	0.843	0.160	Si8	0.568	0.999	0.189
Si9	0.768	0.017	0.204	Si10	0.299	0.807	0.173
Si11	0.184	0.663	0.177	Si12	0.930	0.906	0.176
O1	0.82	0.49	0.21	O2	0.99	0.54	0.21
O3	0.96	0.41	0.28	O4	0.64	0.51	0.23
O5	0.46	0.56	0.23	O6	0.59	0.65	0.20
O7	0.75	0.74	0.19	O8	0.90	0.67	0.20
O9	0.90	0.82	0.19	O10	0.86	0.96	0.22
O11	0.67	0.97	0.22	O12	0.49	0.93	0.19
O13	0.58	0.80	0.20	O14	0.41	0.80	0.19
O15	0.24	0.74	0.21	O16	0.08	0.67	0.21
O17	0.77	0.09	0.28	O18	0.73	0.39	0.29
O19	0.92	0.92	0.07	O20	0.69	0.88	0.00
O21	0.49	0.85	0.05	O22	0.28	0.81	0.06
O23	0.05	0.79	0.01	O24	0.83	0.75	0.04
O25	0.63	0.73	0.05	O26	0.41	0.68	0.03
O27	0.18	0.65	0.07	O28	0.98	0.62	0.06
O29	0.77	0.57	0.04	O30	0.54	0.54	0.08
O31	0.33	0.51	0.07	O32	0.12	0.47	0.08
O33	0.92	0.43	0.09	O34	0.70	0.41	0.11
O35	0.48	0.37	0.08	O36	0.28	0.34	0.11
O37	0.06	0.29	0.13	O38	0.84	0.24	0.08
O39	0.63	0.22	0.10	O40	0.41	0.17	0.09
O41	0.21	0.12	0.10	O42	0.98	0.10	0.07
O43	0.76	0.06	0.10	O44	0.56	0.03	0.09
O45	0.35	0.98	0.07	O46	0.13	0.96	0.06

Atom	x	y	z	PP
Mn1	0.000	0.000	0.000	0.95
Mn2	0.224	0.025	−0.008	0.79
Mn3	0.434	0.069	0.023	0.96
Mn4	0.643	0.123	0.022	0.96
Mn5	0.854	0.139	0.028	0.98
Mn6	0.081	0.176	0.045	0.85
Mn7	0.284	0.225	0.072	1.02
Mn8	0.493	0.255	0.035	0.88
Mn9	0.723	0.293	0.038	1.01
Mn10	0.941	0.316	0.042	1.12
Mn11	0.139	0.355	0.041	1.03
Mn12	0.359	0.397	0.002	0.99
Mn13	0.580	0.429	0.021	1.11
Mn14	0.797	0.450	0.001	1.20
Mn15	0.000	0.000	0.500	0.96

Note: the standard deviation is approximately 0.006 for Si coordinates, 0.008 for Mn coordinates, and 0.01 for O coordinates. The population parameter (PP) was only refined for Mn with a standard deviation of approximately 0.04. Isotropic temperature parameters for the Rietveld refinement and the HRTEM image calculations were fixed at B(Mn) = 0.8, B(Si) = 0.6, and B(O) = 1.2 Å^2.

high electron density and bright areas low electron density, or tunnels, in the structure (Self et al., 1985).

The calculated image, shown as inset in Figure 5, reproduces the dark bands representative of the Mn layers and the brighter bands with sets of three bright blobs in triangles that invert alternately. Comparison of the image with a ball model of the structure in the same projection (Fig. 14) shows that the darkest blobs within the tetrahedral layers occur at locations where two Si atoms superimpose in the projection. These dark blobs are arranged in such a way as to leave inverting triangles white.

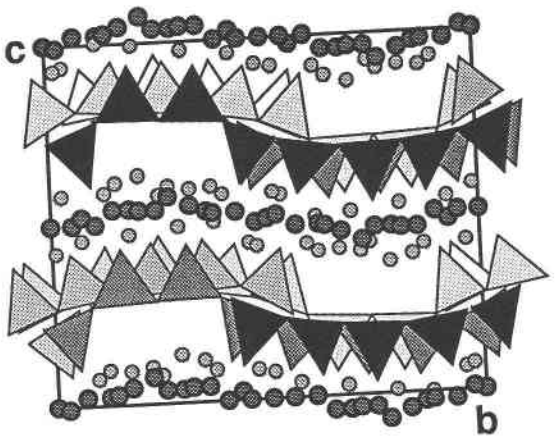

Fig. 13. Projection of the bementite structure onto the **bc** plane (bigger, darker shaded circles = Mn; smaller, lighter shaded circles = OH).

Single Si atoms are faintly visible as smaller dark spots along the edges of the triangles.

The contrast of the (100) fringes is less pronounced in the simulated image than in the one observed in the experimental image. However some of the contrast could be reproduced by shifting the center of the Laue zone to $\overline{1/3}0\,1/3$ for the image calculation. The remaining discrepancy between the experimental and simulated images may be caused by beam tilt or, as in antigorite (Otten, 1993), may be related to the incoherent imaging contribution to long-period features such as the (100) fringes, which is not accounted for by coherent imaging theory.

The [100] projection

Figure 7 shows a [100] projection at defocus settings of +10 and −15 nm, respectively. After the determination of the defocus settings for the experimental images, images of several inclinations of the crystal toward the beam were calculated to correct for the crystal tilt. The calculated images match the experimental images best if the center of the Laue zone is shifted to $02\bar{1}$ for the calculation.

The calculated images show that at the experimental defocus settings the images indeed look like a negative of the Scherzer-focus image. If one compares the experimental images with a ball model of the same projection (Fig. 15), the bright continuous wavy lines represent the Mn layers. The four bright dots (Fig. 7b) along **b** in the tetrahedral sheet can each be interpreted as groups of several Si atoms, superimposed in projection. The dark areas arranged alternately on either side of the dotted line show the tunnels between the basal O atoms and the octahedral sheet.

On the right side of Figure 7, the image shows an area with a wavelength approximately twice the normal **b** re-

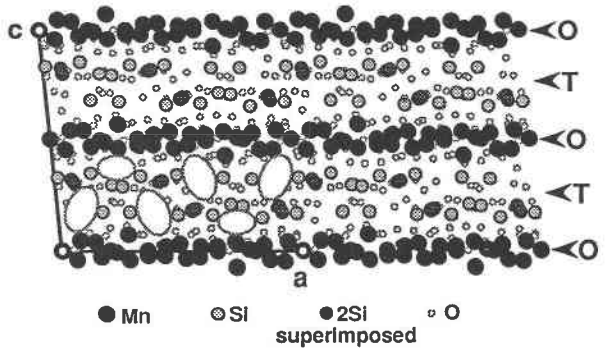

Fig. 14. Ball model of bementite in [010] projection. Pairs of Si atoms that are superimposed in this projection are shaded darker and give rise to the darker blobs in the lighter bands representing the tetrahedral sheet in the HRTEM image of Fig. 5. The areas causing the bright blobs observed in the image are outlined in the lower half of one unit cell.

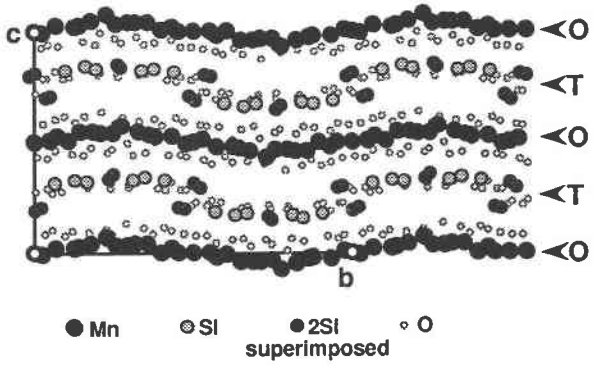

Fig. 15. Ball model of bementite in [100] projection indicating the tunnels, visible as black areas, and the superimposed Si atoms, visible as white dots along the bright line representing the tetrahedral sheet in the HRTEM image of Fig. 7.

peat for the Mn-sheet modulation. This variation in the periodicity along **b** is compatible with the streaking along **b*** in the $0kl$ diffraction pattern and may indicate a minor variation in the composition of the octahedral sheet, e.g., substitution of Fe^{2+} or Mg^{2+} for the larger Mn^{2+}.

The [110] projection

In the image of a projection along [110] (Fig. 8a), the Mn rows parallel to the beam can be distinguished as elongated dots. These rows, which are separated by 2.8 Å (distance d_1 in Fig. 10) are observable only in every second Mn layer. The Mn layers in between show much less contrast, probably because they are not as well aligned with the incident beam. In Figure 8b only rows separated by even numbers of tetrahedral sheets or whole c-cell constants show high contrast, indicating that every octahedral Mn sheet is rotated relative to its neighbor.

Discussion and conclusions

Within the group of modulated layer silicates only pyrosmalite (Kato and Takéuchi, 1983), with an island size of one single six-membered ring, shows a higher ratio between the average radii of octahedral and tetrahedral cations (3.12) than bementite (3.08). Zussmanite (Lopes-Vieira and Zussman, 1969), which, like pyrosmalite, has an island structure with an island size of only a single six-membered ring, has a maximum ratio of approximately 3.0 for Mn-rich varieties. In bementite the tetrahedral six-membered ring strip, comprising two edge-sharing six-membered rings, is too wide to accommodate the existing misfit to the octahedral sheet, and so the bementite structure must have a geometry that can compensate for this misfit along the strip in the **a** direction as well. This is achieved by linking the double six-membered rings along the strip direction by a pair of extra tetrahedra, thus forming seven-membered rings. This breaks up the rigid six-membered ring pattern of the normal layer silicate and allows an elongation of the six-membered rings along **a**, as well as a curling of the double six-membered rings around **b**, thereby spreading the tetrahedral apices farther apart than would be permitted by corrugation of the octahedral sheet alone. Hence the bementite structure should perhaps be regarded as an intermediate between the strip and island structures.

The electron diffraction patterns show that bementite from Franklin is a mixture of two stacking varieties. Variety I dominates the powder pattern and has no stacking

Table 3. Parameters relevant to the Rietveld refinement

2θ range		10.0–60.0°
Step size (2θ)		0.02°
Standard peak for 00l reflections (hkl, 2θ)		004, 24.31°
Standard peak for hkl reflections (hkl, 2θ)		014, 24.85°
Space group		$P2_1/c$
Lattice constants after least-squares refinement (Å)		a = 14.838(2) b = 17.584(2) c = 14.700(2) β = 95.54(2)°
No. of observations (N)		2421
No. of contributing reflections		1052
No. of structural parameters (P1)		228
No. of profile parameters (P2)		10
No. of soft restrictions		392
Residuals		
$R_{exp} = \{(N - P1 - P2)/w_i(I_{io})^2\}^{1/2}$		0.130
	Initial	Final
$R_{wp} = \{\Sigma w_i(I_{io} - I_{ic})^2/\Sigma w_i(I_{io})^2\}^{1/2}$	0.369	0.228
$R_F = \{\Sigma(\lvert F_{io}\rvert - \lvert F_{ic}\rvert)/\Sigma\lvert F_{ic}\rvert\}$	0.168	0.117
$R_D = \{\Sigma w_i(D_{io} - D_{ic})^2/\Sigma w_i(D_{io})^2\}^{1/2}$	0.011	0.027
(D_{io} = prescribed distance between two atoms, D_{ic} = calculated distance between two atoms)		
Soft restrictions		
Distances (Å)		
Si-O		1.623 (weight 50)
Si-Si		3.12 (weight 10)
Mn-O		2.21 (weight 15)
Mn-Mn		3.30 (weight 2)
Angles		
O-Si-O		109.5° (weight 0.5)
O-Mn-O (shared edges)		82° (weight 0.1)
O-Mn-O (unshared edges)		96° (weight 0.1)

faults and a β of 95.5°. Variety II has a stacking fault at every Mn layer, which results in a β of 71.3°. Variety II can only be identified with electron microscopic methods but is confirmed by peaks of low intensity at the predicted positions in the final difference-Fourier map of the Rietveld refinement.

This study exemplifies how the combination of quantitative modeling of HRTEM data with powder XRD refinement can be used to determine, simultaneously, the polytypism as well as the basic structure of materials that show random disorder. Any diffraction pattern from a crystal structure shows the average distance between stacking faults within the coherence area of the radiation (McLaren and MacKenzie, 1976). The optical coherence area of X-rays is significantly smaller than the coherence area of an electron beam. Thus, the fairly long-range random disorder of the stacking faults does not affect the XRD pattern as severely as the electron diffraction pattern. Most of the $h0l$ electron diffraction patterns have the bandlike appearance of a slightly disordered phase, whereas in the XRD pattern the positions of the parent structure reflections are largely maintained, except that the peaks are broadened. Powder XRD refinement therefore allowed the determination of the parent structure of bementite.

Acknowledgments

The sample was kindly provided by the Australian Museum in Sydney. We thank R. Gubser (ETH Zürich) and C. Foudoulis (ANU) for measuring the powder data, and Ch. Baerlocher (ETH Zürich), R. Withers, J. Fitz Gerald, and A. McLaren (ANU) for discussion and critical review. We are grateful to B. Hyde for providing access to the electron microscope facility at the Research School of Chemistry, ANU. We wish to thank the Australian National University for funding this project (grant 90S-ARC-R026). Part of this study was supported by the U.S. National Science Foundation (grant no. EAR-90-03688).

References cited

Amelinckx, S., Van Landuyt, J., and Van Tendeloo, G. (1984) The use of high resolution electron microscopy in the study of modulated structures in alloy systems. In T. Tsakalakos, Ed., Modulated structure materials, p. 183–222. NATO Advanced Science Institute series, Martinus Nijhoff, Amsterdam.

Baerlocher, Ch. (1982) The X-ray Rietveld system: Version of Sept. 1982. Institut für Kristallographie und Petrographie, Eidgenössische Technische Hochschule, Zürich.

Baerlocher, Ch., Hepp, A., and Meier, W.M. (1976) A program for the simulation of crystal structures by geometric refinement, 125 p. Institut für Kristallographie und Petrographie, Eidgenössische Technische Hochschule, Zürich.

Cowley, J.M. (1979) Retrospective introduction: What are modulated structures? A.I.P. Conference Proceedings Nr. 53, p. 1–9. American Institute of Physics, New York.

Cowley, J.M., and Moodie, A.F. (1957) The scattering of electrons by thin crystals. I. A new theoretical approach. Acta Crystallographica, 10, 609–619.

Cruz, M.D.R., and Real, L.M. (1991) Practical determination of allophane and synthetic alumina and iron oxide gels by X-ray diffraction. Clay Minerals, 26, 377–387.

Eggleton, R.A. (1972) The crystal structure of stilpnomelane. II. The full cell. Mineralogical Magazine, 38, 693–711.

Eggleton, R.A., and Guggenheim, S. (1988) A new model for the structure of bementite, a modulated 1:1 layer silicate. Geological Society of America Abstracts With Programs, 20, 7, A358.

Frondel, C., and Baur, L.H. (1955) Kutnahorite: A manganese dolomite: $CaMn(CO_3)_2$. American Mineralogist, 40, 748–760.

Gjønnes, J., and Moodie, A.F. (1965) Extinction conditions in the dynamic theory of electron diffraction. Acta Crystallographica, 19, 65–67.

Goodman, F., and Moodie, A.F. (1974) Numerical evaluation of n-beam wave functions in electron scattering by the multi-slice method. Acta Crystallographica, A30, 280–290.

Guggenheim, S., and Eggleton, R.A. (1987) Modulated 2:1 layer silicates: Review, systematics, and predictions. American Mineralogist, 72, 724–738.

——— (1988) Crystal chemistry, classification, and identification of modulated layer silicates. In Mineralogical Society of America Reviews in Mineralogy, 19, 675–725.

Hefter, J., and Kenney, M.E. (1982) Synthesis of the tube silicate lititidionite and structural relationship between it and some other silicates. Inorganic Chemistry, 21, 2810–2816.

Heinrich, A.R. (1983) Beiträge zur Kristallchemie des Cu(II) in Silikaten, 128 p. Dissertation 7303, Eidgenössische Technische Hochschule, Zürich.

Hepp, A., and Baerlocher, Ch. (1988) Learned peak shape functions for powder diffraction data. Australian Journal of Physics, 41, 229–236.

Ibers, J.A., and Hamilton, W.C., Eds. (1974) International tables for X-ray crystallography, vol. IV, 366 p. Kynoch, Birmingham, England.

Kato, T. (1963) New data on the so called bementite. Mineralogical Journal of Japan, 6, 93–103.

Kato, T., and Takéuchi, Y. (1980) Crystal structures and submicroscopic textures of layered manganese silicates. Mineralogical Journal of Japan, 14, 165–178.

——— (1983) The pyrosmalite group of minerals. I. Structure refinement of manganpyrosmalite. Canadian Mineralogist, 21, 1–6.

Kawamura, K., and Kawahara, A. (1977) The crystal structure of synthetic copper and sodium silicate: $CuNa_2(Si_4O_{10})$. Acta Crystallographica, B33, 1071–1075.

Kunze, G. (1961) Antigorit: Strukturtheoretische Grundlagen und ihre praktische Bedeutung für weitere Serpentin-Forschung. Fortschritte der Mineralogie, 39, 206–335.

Lopes-Vieira, A., and Zussman, J. (1969) Further detail on the structure of zussmanite. Mineralogical Magazine, 37, 49–60.

McLaren, A.C., and MacKenzie, W.S. (1976) The spatial coherence of X-ray and electron beams and its influence on the diffraction patterns from materials with long-period superlattices. Physica Status Solidi, A33, 491–495.

Megaw, H. (1960) Order and disorder: Theory of stacking faults and diffraction maxima. Proceedings of the Royal Society of London, A259, 59–78.

Otten, M.T. (1993) High-resolution transmission electron microscopy of polysomatism and stacking defects in antigorite. American Mineralogist, 78, 75–84.

Self, P.G., Glaisher, R.W., and Spargo, A.E.C. (1985) Interpreting high-resolution transmission electron micrographs. Ultramicroscopy, 18, 49–62.

Smith, D.J., Saxton, W.O., O'Keefe, M.A., Wood, G.J., and Stobbs, W.M. (1983) The importance of beam alignment and crystal tilt in high resolution electron microscopy. Ultramicroscopy, 11, 263–281.

Stadelmann, P.A. (1987) EMS: Software package for electron diffraction analysis and HREM image simulation in materials science. Ultramicroscopy, 21, 131–146.

Strunz, H. (1957) Mineralogische Tabellen (1st edition), 621 p. Geest und Portig, Leipzig, Germany.

Threadgold, I.M. (1979) Ferroan bannisterite: A new type of layer silicate structure: Seminar on Broken Hill (abs.). Mineralogical Society of New South Wales and Mineralogical Society of Victoria, Broken Hill, New South Wales.

Van Landuyt, J. (1991) Electron microscopy of modulated structures. International Workshop on Methods of Structure Analysis of Modulated Structures and Quasi-Crystals, Leikeito, 29 April–4 May 1991.

Manuscript received January 21, 1992
Manuscript accepted September 27, 1993